

# Ordered and tunable Majorana-zero-mode lattice in naturally strained LiFeAs

Meng Li<sup>1,2#</sup>, Geng Li<sup>1,2,3,4#</sup>, Lu Cao<sup>1,2#</sup>, Xingtai Zhou<sup>1,2</sup>, Xiancheng Wang<sup>1,2</sup>, Changqing Jin<sup>1,2,4</sup>, Ching-Kai Chiu<sup>5</sup>, Stephen J. Pennycook<sup>1,2</sup>, Ziqiang Wang<sup>6\*</sup>, and Hong-Jun Gao<sup>1,2,3,4\*</sup>

<sup>1</sup> *Beijing National Center for Condensed Matter Physics and Institute of Physics, Chinese Academy of Sciences, Beijing 100190, PR China*

<sup>2</sup> *School of Physical Sciences, University of Chinese Academy of Sciences, Beijing 100190, PR China*

<sup>3</sup> *CAS Center for Excellence in Topological Quantum Computation, University of Chinese Academy of Sciences, Beijing 100190, PR China*

<sup>4</sup> *Songshan Lake Materials Laboratory, Dongguan, Guangdong 523808, PR China*

<sup>5</sup> *RIKEN Interdisciplinary Theoretical and Mathematical Sciences (iTHEMS), Wako, Saitama 351-0198, Japan*

<sup>6</sup> *Department of Physics, Boston College, Chestnut Hill, MA 02467, USA*

<sup>#</sup>These authors contributed equally to this work.

\*Correspondence to: [hjgao@iphy.ac.cn](mailto:hjgao@iphy.ac.cn); [wangzi@bc.edu](mailto:wangzi@bc.edu)

**Majorana zero modes (MZMs) obey non-Abelian statistics and are considered building blocks for constructing topological qubits<sup>1,2</sup>. Iron-based superconductors with topological band structures have emerged as promising hosting materials, since isolated candidate MZMs in the quantum limit have been observed inside the topological vortex cores<sup>3-9</sup>. However, these materials suffer from issues related to alloying-induced disorder, uncontrolled vortex lattices<sup>10-13</sup> and a low yield of topological vortices<sup>5-8</sup>. Here, we report the formation of an ordered and tunable MZM lattice in naturally-strained stoichiometric LiFeAs by scanning tunneling microscopy/spectroscopy (STM/S). We observe biaxial charge density wave (CDW) stripes along the Fe-Fe and As-As directions in the strained regions. The vortices are pinned on the CDW stripes in the As-As direction and form an ordered lattice. We detect more than 90 percent of the vortices to be topological and possess the characteristics of isolated MZMs at the vortex center, forming an ordered MZM lattice with the density and the geometry tunable by an external magnetic field. Remarkably, with decreasing the spacing of neighboring vortices, the MZMs start to couple with each other. Our findings provide a new pathway towards tunable and ordered MZM lattices as a platform for future topological quantum computation.**

The long quest for Majorana excitations<sup>14-19</sup> has been fueled by recent experimental progress in material platforms where the localized MZM has been observed<sup>16,20-23</sup>. Among these platforms, iron-based superconductors are considered promising for the observation of clean and robust MZMs<sup>3-5</sup>. FeTe<sub>0.55</sub>Se<sub>0.45</sub> was the first iron-based superconductor found to possess topological surface states (TSS)<sup>24,25</sup>. The large  $\frac{\Delta^2}{E_F}$  ratio, where  $\Delta$  is the superconducting (SC) energy gap and  $E_F$  is the Fermi energy, allows the observation of an isolated MZM in the center of a topological vortex<sup>4</sup>, which exhibits nearly quantized plateaus in differential conductance<sup>9</sup>. Later on, stoichiometric iron pnictides were investigated and the existence of MZMs has been verified in CaKFe<sub>4</sub>As<sub>4</sub> (ref. <sup>8</sup>) and LiFeAs (ref. <sup>6</sup>). Very recently, 1D dispersing Majorana modes and MZMs have been observed in the layered 2D superconductors with topological band structures<sup>26-28</sup>. However, these platforms suffer from alloying-induced disorder, uncontrolled vortex lattice and a low yield of topological vortices, hindering their potential applications.

We start with LiFeAs crystal due to its homogeneous bulk electronic structure, well-defined cleaving surface and rich topological band structures<sup>29</sup>. LiFeAs belongs to the tetragonal crystal system, with lattice constants  $a=b=3.8$  Å and  $c=6.3$  Å (Fig. 1a). The As-As atomic direction defines the high-

symmetry lattice orientations ([10] and [01] in Fig. 1b) of the mechanically cleaved nonpolar surface (Extended Data Fig. 1). The existence of strain in the LiFeAs lattice leads to the formation of wrinkles<sup>30</sup> or electronic ordering such as CDWs<sup>31</sup>. We identified such strained regions with a biaxial CDW phase (Fig. 1c), which appears as a coexistence of small periodic ( $2.7 \pm 0.2$  nm) stripe patterns orienting along the Fe-Fe ([11]) direction ( $\text{CDW}_{\text{Fe-Fe}}$ ) and large periodic ( $24.3 \pm 0.9$  nm) stripe patterns orienting along the As-As ([10]) direction ( $\text{CDW}_{\text{As-As}}$ ). To corroborate the effect of the local strain on the formation of the CDWs, we performed atomically-resolved STM imaging of the surface regions with and without the CDWs (Extended Data Fig. 2, Table S1). The distortion of the lattice in the CDW regions reveals the existence of biaxial and shear strain. The observed CDWs are reproducible in different LiFeAs samples and using different STM instruments (Extended Data Fig. 3). Both CDW wavevectors can be clearly resolved in the Fourier transformed (FT) image (Fig. 1d), with an angle of  $45 \pm 1^\circ$ , breaking the  $C_4$  rotation and reflection symmetry of the crystal lattice. Interestingly, the bright stripes of both  $\text{CDW}_{\text{Fe-Fe}}$  and  $\text{CDW}_{\text{As-As}}$  show abnormal splitting and recombination behavior with increasing bias voltages near  $E_F$  (Extended Data Fig. 4), which are accompanied by a  $\pi$ -phase shift in the stripe pattern (Extended Data Fig. 4c,d,k,p). The similar energy-dependent evolution of the stripes indicates that the two CDW phases are coupled with each other. We note that both CDW wavevectors are nondispersive with energy (Extended Data Figs. 4,5), precluding other possibilities such as quasi-particle interference<sup>32,33</sup>.

To investigate the influence of the biaxial CDW phase on the SC behavior, we measure the  $dI/dV$  spectra in different regions. In the unstrained region (black dot in Fig. 1b), the  $dI/dV$  spectrum shows the multigap feature of LiFeAs, with a large gap of  $\sim 5.8$  meV and a small gap of  $\sim 2.9$  meV (black curve in Fig. 1e), consistent with previous reports<sup>10,32,34,35</sup>. In the strained region, the SC gap on the bright stripe ( $2.1 \pm 0.1$  mV) of  $\text{CDW}_{\text{As-As}}$  is smaller than that off the stripe ( $3.4 \pm 0.2$  mV) (brown and yellow curves in Fig. 1e). Importantly, the two CDW orders affect the local superconductivity in very different ways. While the  $\text{CDW}_{\text{As-As}}$  clearly modulates the SC gap size (Fig. 1f, left panel), the  $\text{CDW}_{\text{Fe-Fe}}$  only modulates the intensity of the SC coherence peak without altering the gap size (Fig. 1f, right panel). The modulation of the SC gap suggests a strong coupling of the CDW to the superconductivity. We note that the periodicity of  $\text{CDW}_{\text{As-As}}$  is significantly larger than the SC coherence length (4.8 nm, ref. <sup>36</sup>) in LiFeAs, and the modulation of SC behavior at such large scale is rare. To provide a straightforward visualization of the coupling between the CDW and the superconductivity, we conduct a series of  $dI/dV$  maps at different energies and extract the SC gap values across the region in Fig. 1g. The SC gap map (Fig. 1h) shows clearly the modulation of the SC gap size by  $\text{CDW}_{\text{As-As}}$ .

We then apply an external field of 0.5 T normal to the sample surface, and find magnetic vortices emerging exclusively on the bright stripes of  $\text{CDW}_{\text{As-As}}$  (Fig. 2a). The strong pinning effect of the vortices by the  $\text{CDW}_{\text{As-As}}$  stripes is likely due to the suppressed SC gap in the bright As-As stripe regions. We take  $dI/dV$  spectra across a typical vortex (along the red arrow in Fig. 2a), and find sharp zero-bias conductance peaks (ZBCPs) near the vortex center in the waterfall plot (Fig. 2b) and intensity map (Fig. 2c), together with a novel “X” like feature and discrete peaks on the two sides of the ZBCP. The ZBCP decays without splitting when the tip moves away from the vortex center (Fig. 2c), which is reminiscent of a MZM in the vortex core of other iron-based superconductors with TSS<sup>4,6,8</sup>. To better differentiate the energy positions of the discrete peaks, we show the negative 2<sup>nd</sup> derivative of the waterfall plot (Fig. 2d) and the intensity map (Fig. 2e) of the  $dI/dV$  curves in Fig. 2b,c. A series of discrete vortex core states can be resolved (Fig. 2d,e), suggesting that the vortex is in the quantum limit<sup>4,37</sup>. The spatial evolution of the peak energy of the core states roughly follow straight lines (dashed drop lines in Fig. 2e), as expected for the low-lying Caroli-de-Gennes-Matricon (CdGM) bound states<sup>38-40</sup>. The other vortices exhibit similar spectroscopic features (Extended Data Fig. 6).

In order to determine the energies of the vortex core states, five individual  $dI/dV$  spectra close to the center of the vortex core (red arrows in Fig. 2d) are replotted in Fig. 2f. The discrete vortex core states manifest as peaks marked by the vertical arrows. The CdGM states are bound states inside the SC gap and spatially localized in a vortex core. In an ordinary vortex, the energy of the bound states is half-integer quantized,  $E_j = j \times E_0$ , where  $j = \pm 1/2, \pm 3/2, \dots$  is the total angular momentum quantum number. However, for a topological vortex, the topological Dirac fermion surface states contribute an additional  $\pi$  phase, leading to a half-integer shift in the quantum number of the total angular momentum. As a result, the energy of the CdGM states is integer-quantized,  $E_j = j \times E_0$ , where  $j = 0, \pm 1, \pm 2, \dots$ , in the topological vortex. The average values and the deviations of the core states are summarized in Fig. 2g. Five discrete states at  $-1.76 \pm 0.11$  (L<sub>-2</sub>),  $-0.81 \pm 0.09$  (L<sub>-1</sub>),  $0.00 \pm 0.06$  (L<sub>0</sub>),  $0.86 \pm 0.10$  (L<sub>1</sub>), and  $1.80 \pm 0.13$  (L<sub>2</sub>) meV are extracted, which approximately follow an integer-quantized sequence. Different from conventional CdGM states, the vortex core states exhibit weak spatial dispersions (horizontal black arrows in Fig. 2e and the extracted core states in Fig. 2g). To accurately determine the energy of the L<sub>0</sub> state, we decompose the original  $dI/dV$  spectra into multiple Gaussian-like peaks<sup>7,40</sup> (Extended Data Fig. 7 and left panel in Fig. 2h). Utilizing this approach, we calibrate the L<sub>0</sub> states (right panel in Fig. 2h), and find that they locate at the Fermi energy. The robust ZBCP with a decaying intensity away from the vortex center is strong evidence of a MZM in a topological vortex<sup>4</sup>. The full width at half maximum (FWHM) of the fitted ZBCPs are  $\sim 0.4$  meV, which is comparable to the energy resolution of our instrument (0.3 meV). These results strongly support the existence of MZMs in the vortex

centers.

We then investigate the influence of the CDW stripes on the  $dI/dV$  spectra of the vortices for further understanding of the spatial evolution of the CdGM states. In the negative 2<sup>nd</sup> derivative of the intensity maps of  $dI/dV$  spectra across a topological vortex (Extended Data Fig. 8a), the dispersion happens at positions marked by the horizontal white dashed lines (left panel in Extended Data Fig. 8a). Remarkably, these horizontal lines are in good agreement with the positions of the dark Fe-Fe stripes (see height profile in the right panel in Extended Data Fig. 8a), indicating that the  $CDW_{Fe-Fe}$  has strong influence on the vortex core states. The CdGM states are usually understood as eigenstates of a vortex under rotation symmetry. Once the rotation and reflection symmetries are broken, hybridization between the eigenstates can cause the spatial dispersions of the CdGM states (Fig. 2g and Extended Data Fig. 8b). We note that this is the first experimental observation of hybridization between vortex core states. The MZMs, however, do not disperse and remain at zero-energy, consistent with its topologically protected robustness against local perturbations.

Increasing the external field to 3 T, we observe that more vortices emerge, pinned to the bright  $CDW_{As-As}$  stripes (Extended Data Fig. 9). Figure 3a shows the intensity map of  $dI/dV$  spectra across a topological vortex in the upper panel and an ordinary vortex in the lower panel. Remarkably, its negative 2<sup>nd</sup> derivative shows a half-integer level shift in the energy of the vortex core states (Fig. 3b), which was considered as strong evidence distinguishing the topological vortex and the ordinary vortex<sup>40</sup>. We also plot the individual  $dI/dV$  spectra at the two vortex cores as marked by the red and black dashed lines in Fig. 3a. A sharp ZBCP is seen in the topological vortex (upper panel in Fig. 3c). However, the ZBCP is absent for the ordinary vortex (lower panel in Fig. 3c). We measure the  $dI/dV$  spectra at the center of each topological vortex as shown in Extended Data Fig. 10. All spectra show similar profiles, suggesting the electronic structure of the vortices are uniform. More than 90 percent of vortices are topological vortices, giving rise to an ordered MZM lattice (Extended Data Fig. 10). This conclusion holds for different magnetic fields from 0.5 to 6 T (see Methods, Extended Data Fig. 11 and Extended Data Fig. 12).

Now we discuss the possible origin of the MZM lattice. The topological nature of the pristine LiFeAs is very intriguing and contains two parts. First there is a set of helical Dirac fermion TSS akin to that in a 3D topological insulator, which are located closest to the Fermi level. Second and unique to LiFeAs, there is a set of bulk Dirac fermion states sitting  $\sim 10$  meV above the Fermi level, which is characteristic of a topological Dirac semimetal. This dual topological nature complicates the vortex core spectrum

for the unstrained LiFeAs, which appeared gapless, and prohibited the identification of the discrete vortex core states<sup>6,10,41,42</sup>. To uncover the electronic structure of the strained LiFeAs, we take wide energy scale  $dI/dV$  spectra in the unstrained (lower region in Extended Data Fig. 13) and the  $CDW_{Fe-Fe}$  (upper left region in Extended Data Fig. 13) regions, and in the biaxial CDW region on and off the As-As stripes (Fig. 3d and Extended Data Fig. 15). In the unstrained region, a hump can be recognized at an energy of  $\sim 33$  meV (black curves in Fig. 3d and Extended Data Fig. 14), which is assigned to the top of  $d_{xy}$  band<sup>6</sup>. In the strained regions, however, the hump feature disappears (brown, yellow and blue curves in Fig. 3d and Extended Data Fig. 14), indicating a renormalization in the local electronic structure by the CDW orders. In the uniaxial  $CDW_{Fe-Fe}$  region, the coherence peak of the  $CDW_{Fe-Fe}$  is identified at  $\sim 10$  mV (blue arrow in Fig. 3d), in accordance with previous reports<sup>31</sup>. In the biaxial CDW region, additional peaks indicated by the brown and yellow arrows can be resolved (Fig. 3d and Extended Data Fig. 14). This new peak corresponds to the coherence peak of the  $CDW_{As-As}$  order, since it is strongly modulated by the As-As stripes (Extended Data Fig. 15).

The above assigned CDW coherence peaks, together with the SC coherence peaks, lie on a background of a “V” shaped envelope in the  $dI/dV$  spectra (Fig. 3e and Extended Data Fig. 16) with the dip locating at  $\sim -10$  mV. This V-shaped envelope is a signature for the existence of a Dirac cone<sup>4,43</sup> in two dimensions. These observations together suggest that the most significant changes in the electronic structure in the strained biaxial CDW regions come from the breaking of the rotation and reflection symmetries, which gaps out the bulk Dirac cone protected by the rotation symmetry. This turns the local electronic structure of the stoichiometric, but strained biaxial CDW regions into a strong topological insulator exclusively, hosting the prominent helical Dirac fermion TSS (Fig. 3f) and generates the robust topological Majorana vortices in the SC state. This conclusion is corroborated by the fact that in the unstrained and the uniaxial  $CDW_{Fe-Fe}$  regions, only ordinary vortices with no MZMs are observed (Extended Data Fig. 17).

We finally demonstrate the tunability of the ordered MZM lattice by external magnetic field. The ordered MZM lattice originates from the fact that all vortices are firmly pinned to the periodic bright stripes along the As-As direction (Fig. 4). At 0.5 T, the vortices have relatively low density and arrange themselves amorphously. Upon increasing the magnetic field to 5 T, the MZM lattice gradually evolves into the triangular lattice shape. It should be noted that at -0.5 mV, the vortices are ring-shaped, while at 0 and 0.5 mV they appear as solid circles. The  $dI/dV$  maps reflect the wavefunctions of the bound states inside the vortex cores which are described by Bessel functions<sup>38,44,45</sup>. The ring structure for the negative energy branch suggests that the chemical potential lies above the Dirac point<sup>8,45</sup> (Fig. 3f). The

pinning effect of the vortices by the stripes is so strong that the mobility of the vortices is limited to only one direction – along the stripe. By increasing the field, the newly emerged vortices are “doped” into the bright stripes, forming regular 1D vortex chains. The inter-chain vortex interactions are fixed due to the pinning effect, while the intra-chain vortex interactions can be manipulated by the applied magnetic field (Extended Data Fig. 18). The strong pinning effect provides better control over the vortex motion, as compared to the traditional two-dimensional disordered Abrikosov vortex lattices<sup>10,11</sup>. It is further demonstrated that the ordered lattice is tunable by the external magnetic fields. The overall size of the MZM lattice can be brought up to the micron level, only limited by the STM scanning capability, and could extend to an even larger area (bottom panel of Fig. 4). We have also obtained the correlation between the vortex spacing and the  $dI/dV$  spectra of the vortices, indicating a coupling between the MZMs under high magnetic fields (Extended Data Fig. 19).

In summary, we have observed a micron-scale MZM lattice on naturally strained LiFeAs surface. The vortices are pinned to the  $CDW_{As-As}$  stripes, giving rise to an ordered Abrikosov vortex lattice. We have demonstrated that the ordered lattice is tunable by external magnetic fields and observed the coupling between the MZMs under high magnetic fields. Our findings provide a promising platform for manipulating and braiding MZMs in the future. The large ordered array of MZMs can be suitable for realizing the “braiding by measurement-only” algorithm using interferometry<sup>46</sup>.

## References

1. Kitaev, A. Y. Fault-tolerant quantum computation by anyons. *Ann. Phys-new. York.* **303**, 2-30 (2003).
2. Nayak, C. et al. Non-Abelian anyons and topological quantum computation. *Rev. Mod. Phys.* **80**, 1083-1159 (2008).
3. Zhang, P. et al. Observation of topological superconductivity on the surface of an iron-based superconductor. *Science* **360**, 182-186 (2018).
4. Wang, D. F. et al. Evidence for Majorana bound states in an iron-based superconductor. *Science* **362**, 333-335 (2018).
5. Machida, T. et al. Zero-energy vortex bound state in the superconducting topological surface state of Fe(Se,Te). *Nat. Mater.* **18**, 811-815 (2019).
6. Kong, L. Y. et al. Majorana zero modes in impurity-assisted vortex of LiFeAs superconductor. *Nat. Commun.* **12**, 4146 (2021).
7. Liu, Q. et al. Robust and Clean Majorana Zero Mode in the Vortex Core of High-Temperature Superconductor (Li<sub>0.84</sub>Fe<sub>0.16</sub>)OHFeSe. *Phys. Rev. X* **8**, 041056 (2018).
8. Liu, W. Y. et al. A new Majorana platform in an Fe-As bilayer superconductor. *Nat. Commun.* **11**, 5688 (2020).
9. Zhu, S. Y. et al. Nearly quantized conductance plateau of vortex zero mode in an iron-based superconductor. *Science* **367**, 189-192 (2020).
10. Hanaguri, T. et al. Scanning tunneling microscopy/spectroscopy of vortices in LiFeAs. *Phys. Rev. B* **85**, 214505 (2012).
11. Fente, A. et al. Influence of multiband sign-changing superconductivity on vortex cores and vortex pinning in stoichiometric high- $T_c$  CaKFe<sub>4</sub>As<sub>4</sub>. *Phys. Rev. B* **97**, 134501 (2018).
12. Chiu, C. K. et al. Scalable Majorana vortex modes in iron-based superconductors. *Sci. Adv.* **6**, eaay0443 (2020).
13. Zhang, S. T. S. et al. Vector field controlled vortex lattice symmetry in LiFeAs using scanning tunneling microscopy. *Phys. Rev. B* **99**, 161103 (2019).
14. Kitaev, A. Y. Unpaired Majorana fermions in quantum wires. *Phys. Uspekhi* **44**, 131-136 (2001).
15. Read, N. & Green, D. Paired states of fermions in two dimensions with breaking of parity and



time-reversal symmetries and the fractional quantum Hall effect. *Phys. Rev. B* **61**, 10267-10297 (2000).

16. Fu, L. & Kane, C. L. Superconducting proximity effect and Majorana fermions at the surface of a topological insulator. *Phys. Rev. Lett.* **100**, 096407 (2008).
17. Lutchyn, R. M., Sau, J. D. & Das Sarma, S. Majorana Fermions and a Topological Phase Transition in Semiconductor-Superconductor Heterostructures. *Phys. Rev. Lett.* **105**, 077001 (2010).
18. Oreg, Y., Refael, G. & von Oppen, F. Helical Liquids and Majorana Bound States in Quantum Wires. *Phys. Rev. Lett.* **105**, 177002 (2010).
19. Potter, A. C. & Lee, P. A. Multichannel Generalization of Kitaev's Majorana End States and a Practical Route to Realize Them in Thin Films. *Phys. Rev. Lett.* **105**, 227003 (2010).
20. Mourik, V. et al. Signatures of Majorana Fermions in Hybrid Superconductor-Semiconductor Nanowire Devices. *Science* **336**, 1003-1007 (2012).
21. Nadj-Perge, S. et al. Observation of Majorana fermions in ferromagnetic atomic chains on a superconductor. *Science* **346**, 602-607 (2014).
22. Xu, J. P. et al. Experimental Detection of a Majorana Mode in the core of a Magnetic Vortex inside a Topological Insulator-Superconductor  $\text{Bi}_2\text{Te}_3/\text{NbSe}_2$  Heterostructure. *Phys. Rev. Lett.* **114**, 017001 (2015).
23. Deng, M. T. et al. Majorana bound state in a coupled quantum-dot hybrid-nanowire system. *Science* **354**, 1557-1562 (2016).
24. Wang, Z. J. et al. Topological nature of the  $\text{FeSe}_{0.5}\text{Te}_{0.5}$  superconductor. *Phys. Rev. B* **92**, 115119 (2015).
25. Wu, X. X. et al. Topological characters in  $\text{Fe}(\text{Te}_{1-x}\text{Se}_x)$  thin films. *Phys. Rev. B* **93**, 115129 (2016).
26. Yuan, Y. H. et al. Evidence of anisotropic Majorana bound states in 2M- $\text{WS}_2$ . *Nat. Phys.* **15**, 1046-1051 (2019).
27. Kezilebieke, S. et al. Topological superconductivity in a van der Waals heterostructure. *Nature* **588**, 424-428 (2020).
28. Nayak, A. K. et al. Evidence of topological boundary modes with topological nodal-point superconductivity. *Nat. Phys.* **17**, 1413–1419 (2021).

29. Zhang, P. et al. Multiple topological states in iron-based superconductors. *Nat. Phys.* **15**, 41-47 (2019).
30. Cao, L. et al. Two distinct superconducting states controlled by orientation of local wrinkles in LiFeAs. *Nat. Commun.* **12**, 6312 (2021).
31. Yim, C. M. et al. Discovery of a strain-stabilised smectic electronic order in LiFeAs. *Nat. Commun.* **9**, 2602 (2018).
32. Allan, M. P. et al. Anisotropic Energy Gaps of Iron-Based Superconductivity from Intraband Quasiparticle Interference in LiFeAs. *Science* **336**, 563-567 (2012).
33. Allan, M. P. et al. Identifying the 'fingerprint' of antiferromagnetic spin fluctuations in iron pnictide superconductors. *Nat. Phys.* **11**, 177-182 (2015).
34. Chi, S. et al. Scanning Tunneling Spectroscopy of Superconducting LiFeAs Single Crystals: Evidence for Two Nodeless Energy Gaps and Coupling to a Bosonic Mode. *Phys. Rev. Lett.* **109**, 087002 (2012).
35. Umezawa, K. et al. Unconventional Anisotropic s-Wave Superconducting Gaps of the LiFeAs Iron-Pnictide Superconductor. *Phys. Rev. Lett.* **108**, 037002 (2012).
36. Zhang, J. L. et al. Upper critical field and its anisotropy in LiFeAs. *Phys. Rev. B* **83**, 174506 (2011).
37. Hayashi, N., Isoshima, T., Ichioka, M. & Machida, K. Low-lying quasiparticle excitations around a vortex core in quantum limit. *Phys. Rev. Lett.* **80**, 2921-2924 (1998).
38. Caroli, C., Degennes, P. G. & Matricon, J. Bound Fermion States on a Vortex Line in a Type-II Superconductor. *Phys. Lett.* **9**, 307-309 (1964).
39. Fan, P. et al. Observation of magnetic adatom-induced Majorana vortex and its hybridization with field-induced Majorana vortex in an iron-based superconductor. *Nat. Commun.* **12**, 1348 (2021).
40. Kong, L. Y. et al. Half-integer level shift of vortex bound states in an iron-based superconductor. *Nat. Phys.* **15**, 1181-1187 (2019).
41. Zhang, S. S. et al. Field-free platform for Majorana-like zero mode in superconductors with a topological surface state. *Phys. Rev. B* **101**, 100507 (2020).
42. Hu, L. H., Wu, X. X., Liu, C. X. & Zhang, R. X. Competing Vortex Topologies in Iron-based Superconductors. *arXiv:2110.11357* (2021).

- 43. Zhang, Y. B. et al. Giant phonon-induced conductance in scanning tunnelling spectroscopy of gate-tunable graphene. *Nat. Phys.* **4**, 627-630 (2008).
- 44. Cheng, M., Lutchyn, R. M., Galitski, V. & Das Sarma, S. Tunneling of anyonic Majorana excitations in topological superconductors. *Phys. Rev. B* **82**, 094504 (2010).
- 45. Kawakami, T. & Hu, X. Evolution of Density of States and a Spin-Resolved Checkerboard-Type Pattern Associated with the Majorana Bound State. *Phys. Rev. Lett.* **115**, 177001 (2015).
- 46. Bonderson, P., Freedman, M. & Nayak, C. Measurement-only topological quantum computation via anyonic interferometry. *Ann. Phys-new. York.* **324**, 787-826 (2009).

## Methods

### Single-crystal growth

High-quality LiFeAs single crystals were synthesized by using the self-flux method. A LiFeAs crystal was mounted on a STM sample holder in a glove box and transferred to an ultra-high vacuum chamber. The crystal was cleaved *in-situ*. The low cleaving temperature of 10 K is for a higher chance to find the strained regions hosting the CDWs compared with the room-temperature cleavage. After cleavage, the sample was immediately transferred to the STM scanner.

### STM/S experiments

The STM/S measurements were conducted in an ultra-low temperature STM system equipped with 9-2-2 T vectorial magnets. Tungsten tips were etched chemically and calibrated on Au(111) surfaces before use. The  $dI/dV$  spectra and maps were obtained by a standard lock-in technique with a modulation voltage of 0.1 mV at 973.0 Hz. All the images, spectra and  $dI/dV$  maps were taken at 400 mK.

### Fitting method

Linear least square fitting was used to determine the positions of the vortex core states. Five Gaussian peaks representing the in-gap bound states were used for the fitting of each spectrum. In the fitting process, all the parameters of the Gaussian peaks are set free. The peak positions of the bound states were extracted from the fitting results.

### Statistics of the topological vortices

The determination of percentage of topological vortices in the biaxial CDW region was performed by the measurement of  $dI/dV$  spectra of 51 vortices under 3 T. A relatively smaller region that contains 3 to 4 vortices within the area were mapped at zero energy so that the centers of the vortex cores could be accurately located. The spectra were all taken under the same scanning settings. The spectra were further calibrated by the multi-Gaussian peak fitting method to accurately locate the positions of the bound states. The same strategy was used for different fields from 0.5 to 6 T, and the topological vortices were always higher than 90% of the total number.

**Acknowledgements:** We thank G. Su and H. Ding for helpful discussions. The work is supported by the Ministry of Science and Technology of China (2019YFA0308500, 2018YFA0305700, 2017YFA0206303), the National Natural Science Foundation of China (61888102, 51991340, 52072401), the Chinese Academy of Sciences (XDB28000000, XDB30000000, 112111KYSB20160061), and the CAS Project for Young Scientists in Basic Research (YSBR-003). Z.W. is supported by the US DOE, Basic Energy Sciences Grant No. DE-FG02-99ER45747.

**Author Contributions:** H.-J.G. designed the experiments and supervised the project. X.W. and C.J. prepared samples. M.L., G.L., L.C. and X.Z. performed STM experiments with guidance of H.-J.G. G.L., C.-K.C, S.J.P., Z.W. and H.-J.G. did data analysis and wrote the manuscript. All of the authors participated in analysing experimental data, plotting figures, and writing the manuscript.

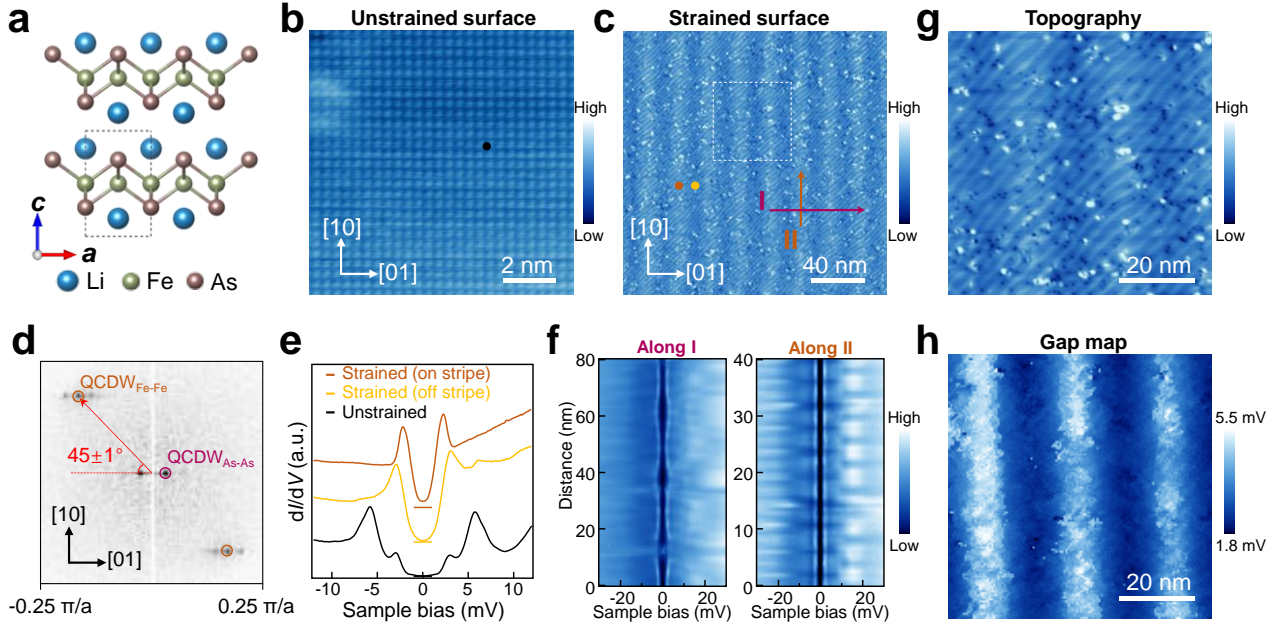


**Fig. 1 | Crystalline structure, topographic image and superconducting behavior of the unstrained and strained regions.** **a**, Atomic model of the LiFeAs single crystal. **b,c**, STM images of unstrained (**b**) and strained (**c**) regions on a cleaved LiFeAs single crystal, respectively (scanning settings for (**b**): bias  $V_s = -3$  mV, setpoint  $I_t = 400$  pA; for (**c**):  $V_s = -30$  mV,  $I_t = 50$  pA). **d**, FT image of **c**, showing the wavevectors of the  $CDW_{Fe-Fe}$  and  $CDW_{As-As}$ . The angle between the wavevectors of  $CDW_{Fe-Fe}$  and  $CDW_{As-As}$  is  $45 \pm 1^\circ$ . **e**, Typical  $dI/dV$  spectra taken at the bright stripe (brown curve), off the bright stripe (yellow curve) of the  $CDW_{As-As}$  and in the unstrained region (black curve). The  $dI/dV$  spectra are vertically offset for clarity, and the horizontal solid lines represent positions of zero density of states for each of the curves. The bright stripe region has smaller SC gap size and higher in-gap density of states compared with that of the off-stripe region. **f**, Intensity maps of the  $dI/dV$  spectra along arrows I (left panel) and II (right panel) in **c**. The SC gap value is modulated by the large stripes of the  $CDW_{As-As}$ , while the  $CDW_{Fe-Fe}$  pattern modulates only the height of SC coherence peaks. **g**, Zoom-in STM image of the white dashed box in **c** ( $V_s = -30$  mV,  $I_t = 50$  pA). **h**, SC gap map of the same region in **g**, showing reduced SC gap sizes on the bright As-As stripes.

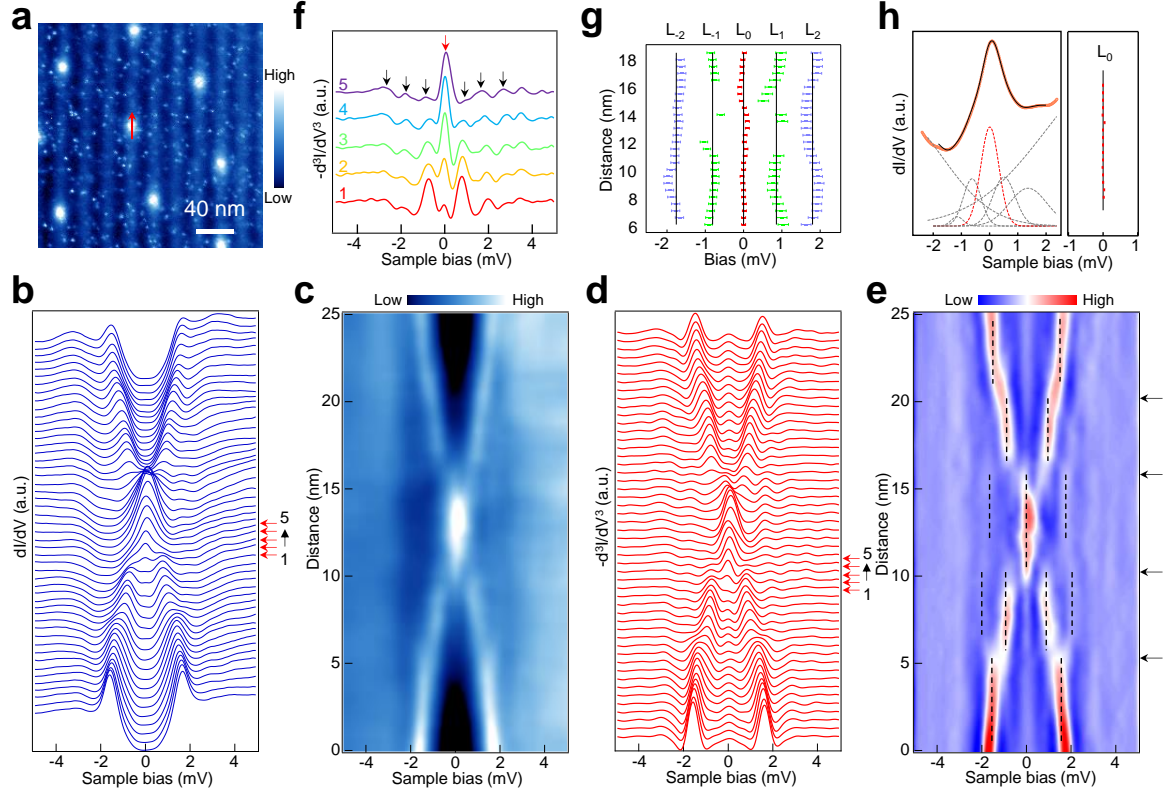


**Fig. 2 |  $dI/dV$  map of the vortices and the analysis of the vortex bound states under 0.5 T.** **a**,  $dI/dV$  map of the biaxial CDW region ( $V_s=0$  mV), showing that the vortices are pinned to the bright As-As stripes. **b,c**, Waterfall plot (**b**) and intensity map (**c**) of the  $dI/dV$  spectra along the red arrow in **a**, showing sharp ZBCP at the center of the vortex. **d,e**, Negative 2<sup>nd</sup> derivative of **b** and **c**, respectively, indicating that a series of discrete peaks locate on the two sides of the ZBCP. The dashed drop lines in **e** outline the positions of the discrete peaks. Following the dashed drop lines, the spatial evolvement of the discrete peaks is divided into sections, as marked by the horizontal black arrows. The peak positions show slight spatial dispersion from straight lines. **f**, Negative 2<sup>nd</sup> derivative of the 5 typical  $dI/dV$  spectra (arrowed in red in **d**) taken close to the center of the vortex in **a**. The ZBCP is highlighted by a vertical red arrow, and the other discrete energy bound states are highlighted by vertical black arrows. **g**, Statistical analysis of the peak positions in **e**. Five energy bound states at  $-1.76 \pm 0.11$  ( $L_{-2}$ ),  $-0.81 \pm 0.09$  ( $L_{-1}$ ),  $0.00 \pm 0.06$  ( $L_0$ ),  $0.86 \pm 0.10$  ( $L_1$ ), and  $1.80 \pm 0.13$  ( $L_2$ ) meV are extracted. **h**, Left panel: the black circles show a typical  $dI/dV$  spectrum near the vortex core, with the extracted  $L_0$  state from **d** deviating from zero energy. The red peak is the calibrated ZBCP by multi-Gaussian peak fitting. The grey lines indicate the fitted CdGM states and the background. The black solid line is the fitted curve. Right panel: spatial distribution of the calibrated  $L_0$  state, showing robust ZBCPs.

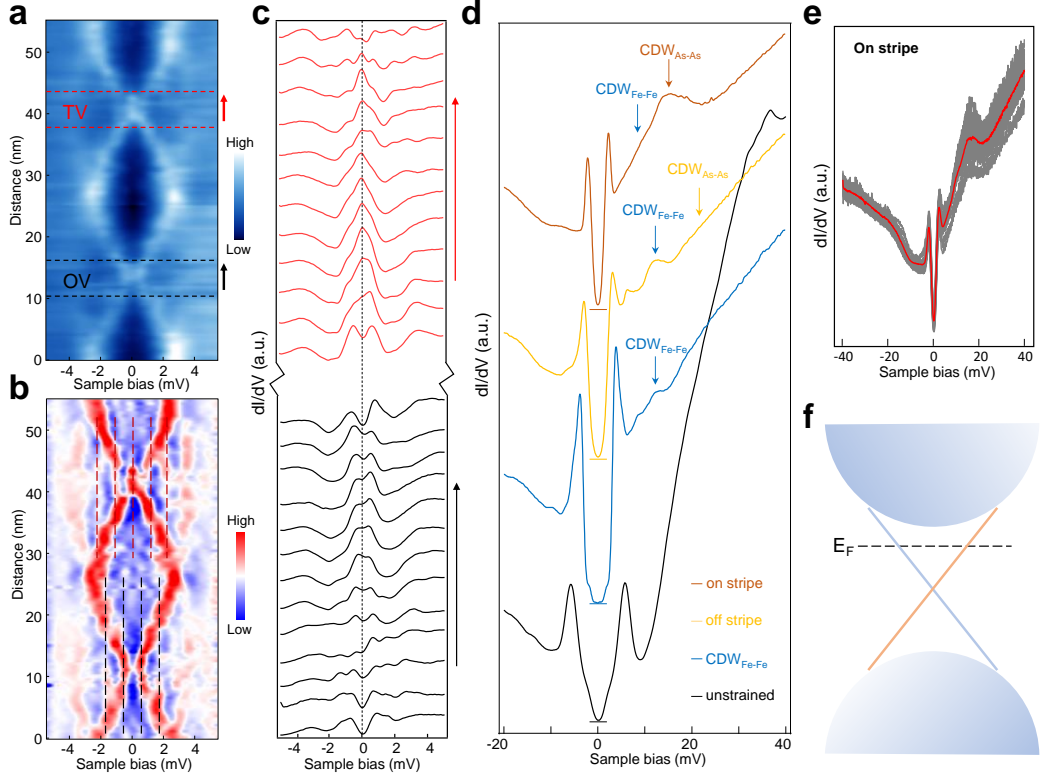


**Fig. 3 | Analysis of the  $dI/dV$  spectra along a linecut across two neighboring vortices and the origin of the MZMs.** **a**, Intensity plot of  $dI/dV$  spectra across two neighboring vortices along a  $CDW_{As-As}$  stripe under 3 T. **b**, Negative 2<sup>nd</sup> derivative of **a**. The vertical dashed lines highlight the vortex core states. The upper vortex is topological with a ZBCP, while the lower vortex is ordinary. The discrete peaks of the ordinary vortex show half-integer level shift with that of the topological vortex. **c**, Zoom-in of the individual  $dI/dV$  spectrum taken at regions close to the two vortex cores, as marked by the horizontal red and black dashed lines in **a**. The vertical black dashed line labels the zero bias. **d**, Wide-range  $dI/dV$  spectra at the on As-As stripe (brown) and off As-As stripe (yellow) locations in a biaxial CDW region, the uniaxial  $CDW_{Fe-Fe}$  region (blue), and the unstrained region (black), respectively. The horizontal solid lines highlight the positions of zero density of states for each curve. The big hump at  $\sim 33$  mV of the black curve assigned to the band top of  $d_{xy}$  in the unstrained region is absent in the uniaxial  $CDW_{Fe-Fe}$  and biaxial CDW regions, suggesting significant band renormalization effects that also reduce the slope of the density states increase with energy. The coherence peaks of  $CDW_{As-As}$  and  $CDW_{Fe-Fe}$  are highlighted by vertical arrows. **e**, Averaged  $dI/dV$  spectra taken on the bright As-As stripes in the biaxial CDW region. The linear dispersion of the TSS can be related to an approximately V-shaped spectral shape with the Dirac point located  $\sim -10$  meV. **f**, Schematics of the band structure of the strained LiFeAs around the  $\Gamma$  point. The bulk states are gapped out by the biaxial CDW order, giving rise to the TI surface states.



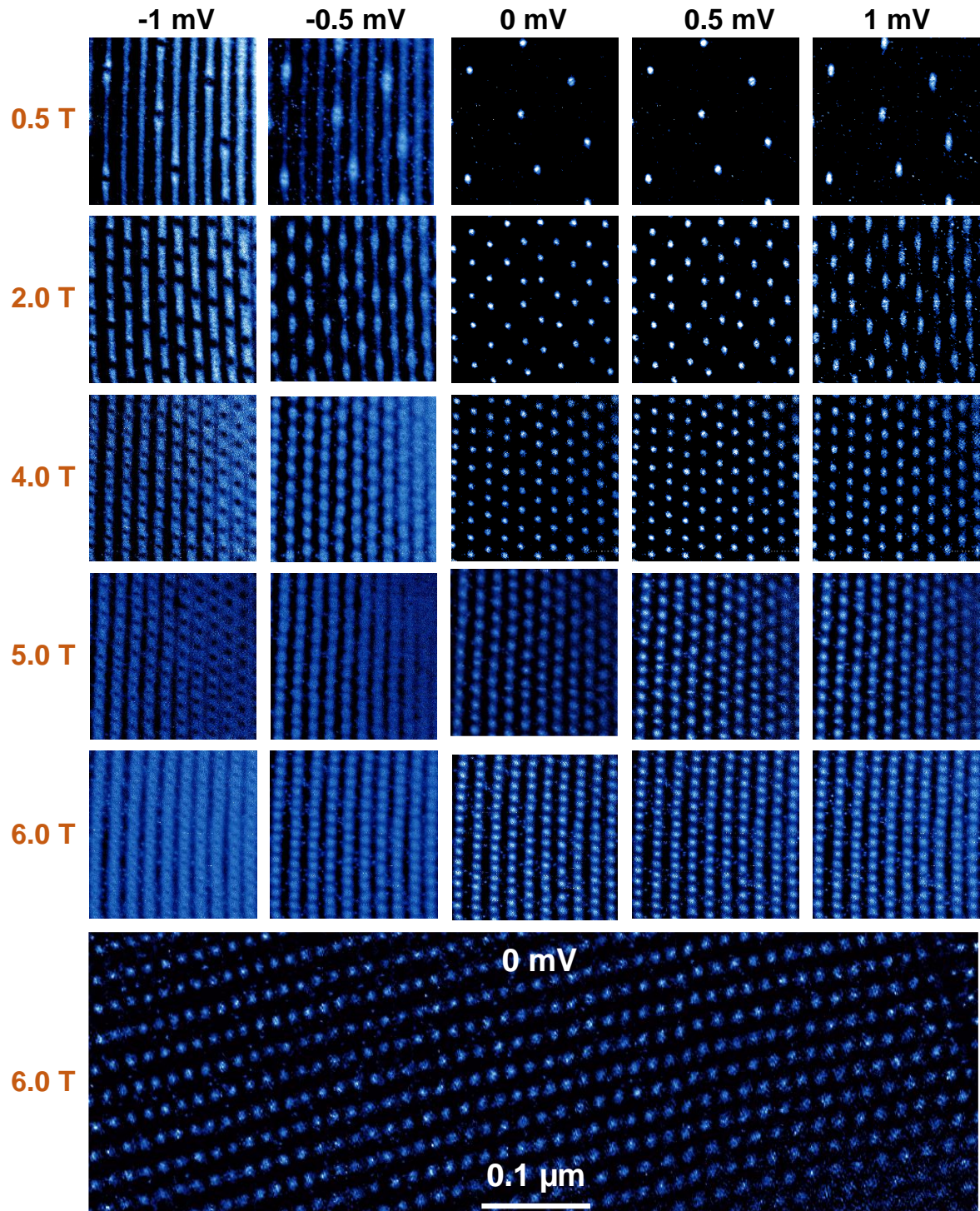


**Fig. 4 | Tuning the MZM lattice with external magnetic fields.** Series of  $dI/dV$  maps of the MZM vortices in the biaxial CDW region under magnetic fields of 0.5 T, 2 T, 4 T, 5 T and 6 T and at bias voltages from -1.0 mV to 1.0 mV, respectively. Large-scale, ordered MZM lattice of different spacing and density is formed when increasing external magnetic fields. The scanning areas are  $0.24 \mu\text{m} \times 0.24 \mu\text{m}$ . Bottom panel: Micron-size ordered MZM lattice under 6 T. The scanning area is  $0.26 \mu\text{m} \times 0.82 \mu\text{m}$ .